



## Molten salts synthesis of NbB nanoparticles for lithium-ion capacitor applications

Jing-Feng Hou<sup>a,b</sup>, Jian-Fei Gao<sup>a,b</sup>, Ling-Bin Kong<sup>a,b,\*</sup>

<sup>a</sup> State Key Laboratory of Advanced Processing and Recycling of Non-ferrous Metals, Lanzhou University of Technology, Lanzhou 730050, PR China

<sup>b</sup> School of Materials Science and Engineering, Lanzhou University of Technology, Lanzhou 730050, PR China

### ARTICLE INFO

#### Keywords:

Lithium-ion capacitors  
Energy storage mechanism  
Electrochemical performance  
Niobium monoboride

### ABSTRACT

Lithium-ion capacitors (LICs), despite having great energy density and power density, possess many practical challenges, including matching optimization of kinetic imbalance. To address the issues, here, niobium monoboride (NbB) nanoparticles are presented as an anode material for LICs. The abundant pore size distribution and intercalation-type  $\text{Li}^+$  storage mechanism of NbB nanoparticles allow for fast redox kinetics in charge and discharge process. Therefore, the half-cells with NbB achieve excellent electrochemical performance, including a great capacity ( $197 \text{ mAh g}^{-1}$  at  $0.1 \text{ A g}^{-1}$  for 1000 cycles) and superior cycle life ( $118 \text{ mAh g}^{-1}$  at  $1 \text{ A g}^{-1}$  for 5000 cycles). Also, NbB//AC LIC-1 device fabricated with the NbB as anode and commercial activated carbon (AC) as cathode reveals a great specific capacitance of  $28.1 \text{ F g}^{-1}$  at  $0.05 \text{ A/g}$ , and remains over 70 % initial capacitance after 12,000 cycles. In this work, nanoscale NbB presents excellent lithium storage performance and matches well with carbon cathodes, indicating that transition metal borides (TMBs) have huge potential in the energy storage field.

### 1. Introduction

With the development of the economy and the continuous innovation of science and technology, it is urgent to develop efficient and stable energy storage devices [1,2]. LICs have attracted extensive attention because of their combination of energy storage characteristics of lithium-ion battery and supercapacitor [3–5]. To meet demand of great energy density, stable cyclic durability and excellent rate capability, people have invested a lot of energy in exploring cathode materials with rapid kinetics process and good matching with negative carbon materials to improve the electrochemical performance of the equipment [6–8].

In recent years, in order to construct high-performance LICs, the negative electrodes of lithium-ion batteries have been widely studied [9]. According to the energy storage mechanism, the negative materials can be divided into intercalation-, alloy- and conversion-typed electrodes. Carbon materials are the typical intercalation-typed electrode, which has been commercialized because of low cost, good conductivity and stable performance [10]. Due to its unique layered structure, graphite electrodes display a remarkable theoretical specific capacity of  $372 \text{ mAh g}^{-1}$ , which makes  $\text{Li}^+$  easy to embed and remove [11].

$\text{Li}_4\text{Ti}_5\text{O}_{12}$  material is also a promising intercalation-typed electrode, which has low volume expansion during charge and discharge, thus showing good cycle life and ultra-fast charge and discharge rate [12]. However, the low theoretical specific capacity and poor conductivity limit the practical applications, so it is necessary to improve the performance of  $\text{Li}_4\text{Ti}_5\text{O}_{12}$  by ion-doping and so on [13]. Conversion-typed electrodes store lithium through conversion reactions. Most transition metal oxide and sulfide electrodes are conversion materials [14,15]. For example, metal oxides are converted to metals and  $\text{Li}_2\text{O}$  in the lithium storage process, which can obtain a higher reversible specific capacity. However, the conversion-typed electrode is easily affected by the capacity decrease caused by volume expansion, so it is necessary to construct a porous nanostructure or form composites with carbon to buffer the large volume change in the cycle process [16,17]. The alloy-typed electrodes are usually formed alloys with lithium metal for energy storage, but the overload of Li can lead to the collapse of the skeleton structure, so it is necessary to prepare mixed electrodes to solve the above problems [18,19].

Currently, TMBs have attracted the interest of scientists because of their multifaceted M-M, M-B, and B-B bond features [20]. Therefore, TMBs possess many unique physicochemical properties such as high

\* Corresponding author at: State Key Laboratory of Advanced Processing and Recycling of Non-ferrous Metals, Lanzhou University of Technology, Lanzhou 730050, PR China.

E-mail address: [konglb@lut.edu.cn](mailto:konglb@lut.edu.cn) (L.-B. Kong).

electrical conductivity, magnetism, superconductivity, chemical stability, as well as rich electroactive sites [21]. Because of their unique crystal structure, TMBs also present the shortened path of ion diffusion, which improves the utilization of electroactive sites, making them outstanding electrode materials for energy storage and conversion [22]. Behera et al. [23] presented an effective redox approach to transform the crystalline Ni-MOF to amorphous NiB, which shows excellent electrocatalytic performance (deliver current density of  $10 \text{ mA cm}^{-2}$  at 240 mV), great specific capacitance, remarkable energy and power density and superior cycle stability (85.45 % capacitance retention for 5000 cycles). Shajumon et al. [24] reported that TiB<sub>2</sub>-derived nanosheets as Na<sup>+</sup> battery anode deliver a discharge capacity of 252 mAh/g at 0.1 A/g, achieving great cycle durability at 1 A/g.

Inspired by this research, we report for the first time that NbB nanoparticles synthesized in NaCl-KCl molten salts are used as LICs anode. The NbB half-cell delivers an excellent specific capacity of 197 mAh/g at 0.1 A g<sup>-1</sup> for 1000 cycles. Upon increasing the rate to 1 A/g, the great capacity of 118 mAh/g can be maintained for 5000 cycles. Further, the LICs device is assembled with NbB as anode and AC as cathode. The NbB//AC LIC-1 device displays great specific capacitance of  $28.1 \text{ F g}^{-1}$  at 0.05 A/g, and outstanding cycle life of 70 % capacitance retention after 12,000 cycles. The study exemplifies the great potential of NbB as negative electrode of LICs and confirms the theoretical prediction on using TMB-based electrode materials for energy storage.

## 2. Results and discussion

The diagram of the synthesis process of NbB sample is exhibited in Fig. 1a. Commercial Nb<sub>2</sub>O<sub>5</sub> and amorphous B are selected as sources of niobium and boron, respectively [25]. The XRD patterns of the products obtained at different experiment conditions are exhibited in Fig. 1b. According to the chemical equation:

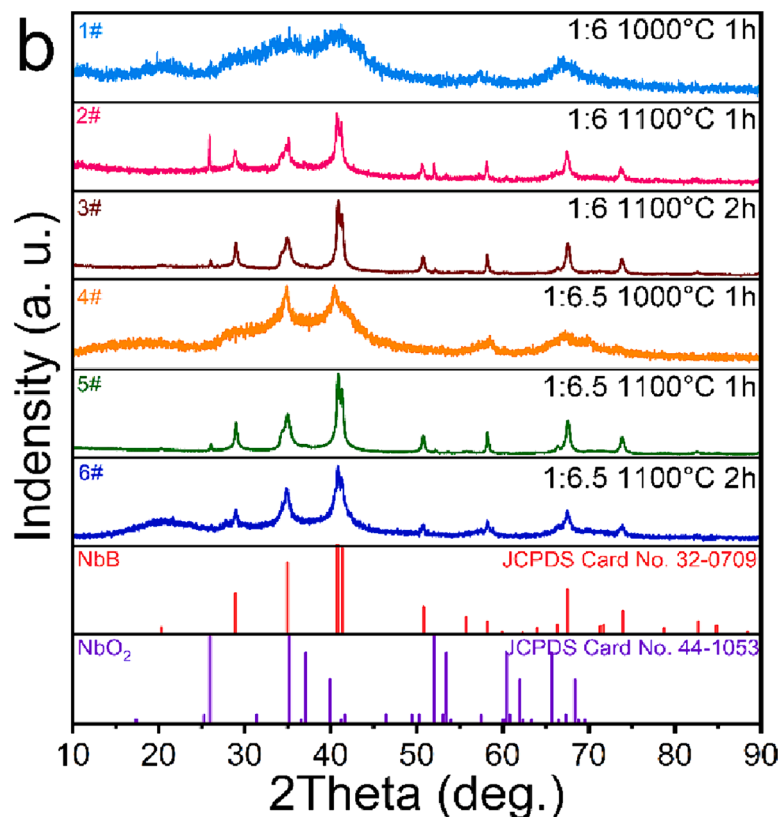
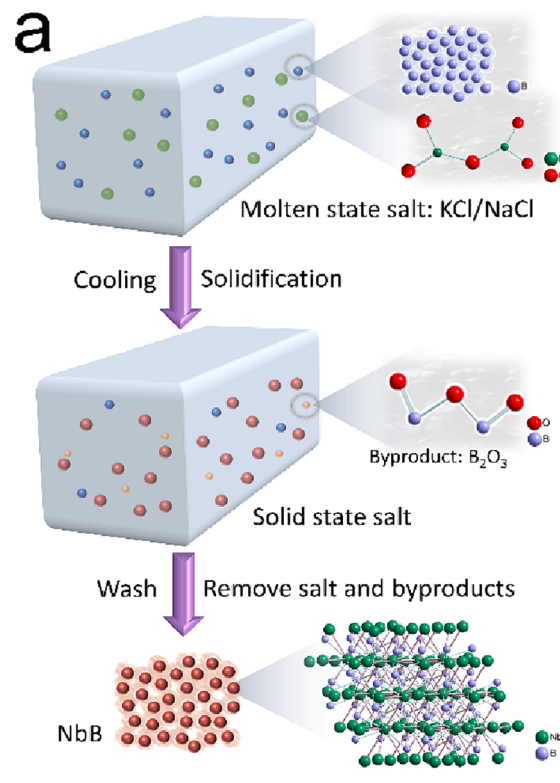
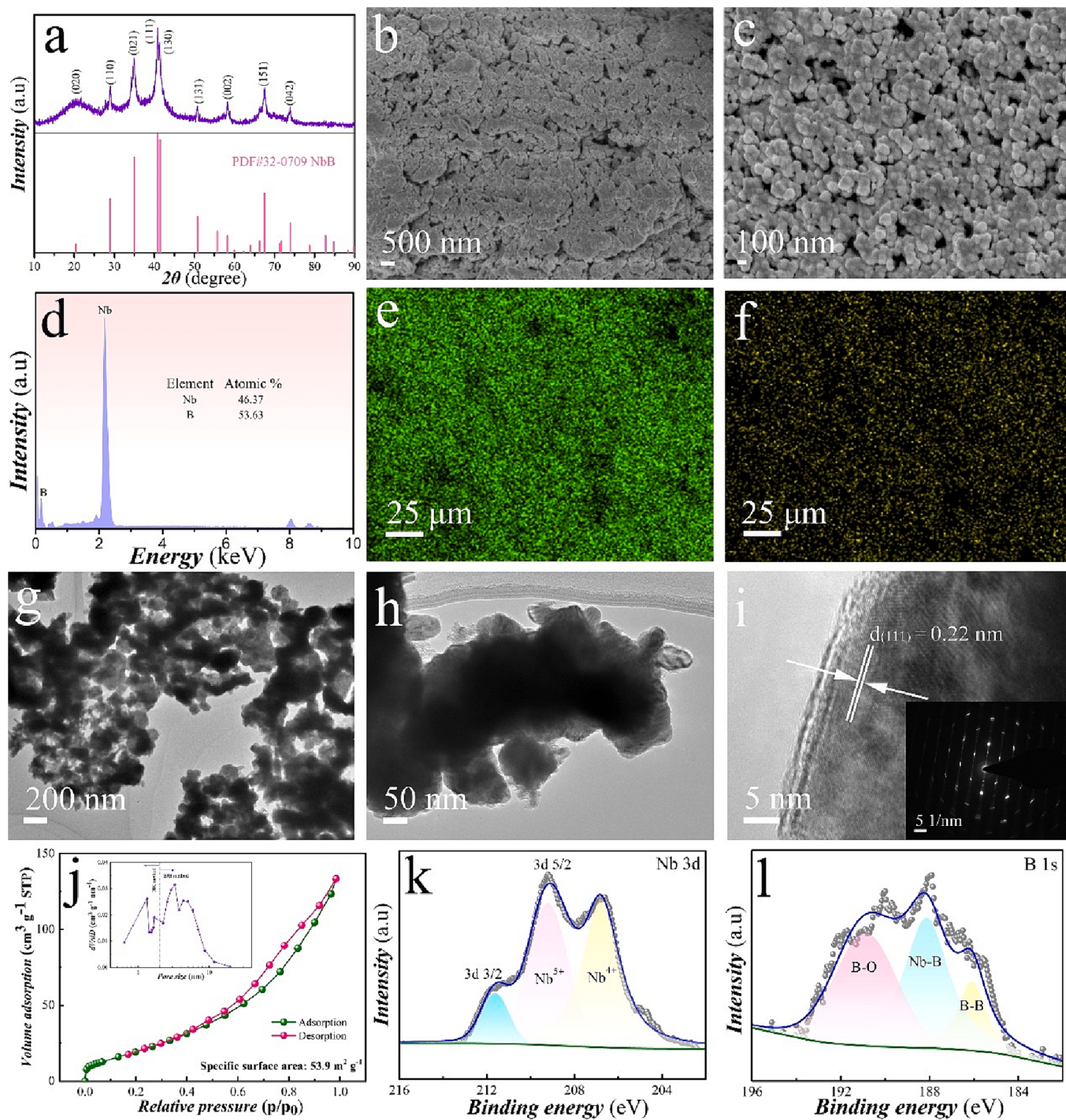


Fig. 1. (a) Diagram of synthesis process of NbB sample, (b) XRD patterns of samples with different synthesis conditions.

considering that a small amount of B escapes during synthesis process, the molar ratio of Nb<sub>2</sub>O<sub>5</sub>: B is set as 1:6. When the synthesis condition is 1000 °C for 1 h, the sample is 1# and shows poor crystallinity. When the temperature is increased to 1100 °C, the NbB phase appears in the resulting 2# sample, but there are some impurities of NbO<sub>2</sub>. When the reaction time is extended to 2 h at 1100 °C, the product 3# sample is still NbB sample containing impurity NbO<sub>2</sub>, but the intensity of NbO<sub>2</sub> diffraction peaks is lower than that of 2#, indicating that the extension of the reaction time can improve the completion degree of the reaction and make Nb<sub>2</sub>O<sub>5</sub> and B fully react. Next, the ratio of B is increased, and tests are carried out with a molar ratio of Nb<sub>2</sub>O<sub>5</sub>: B of 1:6.5. The crystallinity of the 4# sample kept at 1000 °C for 1 h is also poor. When the temperature reaches 1100 °C, it can be observed that Nb<sub>2</sub>O<sub>5</sub> is reduced to NbB and NbO<sub>2</sub> by B in sample 5#. Extending the reaction time, it is found that the NbO<sub>2</sub> phase disappears and Nb<sub>2</sub>O<sub>5</sub> is completely converted into NbB phase, which indicates that the preparation of NbB is successful.

Fig. 2a exhibits the XRD pattern of the NbB product, and all diffraction peaks correspond to PDF# 32-0709. The morphology and microstructure of NbB material are characterized by scanning electron microscopy (SEM). In Fig. 2b-c, NbB sample is formed by aggregating nanoparticles with a diameter of about 100 nm. In the energy dispersive spectroscopy (EDS) diagram exhibited in Fig. 2d, the signals of Nb and B elements can be seen, and the atomic ratio of Nb to B is 46.37: 53.63, which is close to 1: 1. The EDS elemental mapping in Fig. 2e-f further reveal the uniform distribution of Nb and B in the NbB nanoparticles. As shown in Fig. 2g-h, the corresponding transmission electron microscopy (TEM) images of NbB also show that it has agglomerated nanoparticle morphology. The lattice fringes of NbB nanoparticles can be clearly seen in high-resolution TEM (HRTEM) image of Fig. 2i, and the lattice fringes with an interval of 0.22 nm are related to the (111) crystal plane of the NbB. The illustration is selected area electron diffraction (SAED) graph of NbB sample, which displays a series of diffraction spots, indicating the



**Fig. 2.** (a) XRD pattern, (b-c) SEM graphs, (d) EDS pattern, (e-f) element mapping graphs, (g-h) TEM images, (i) HRTEM image, (j) N<sub>2</sub> adsorption–desorption isotherms, (k-l) XPS spectra of the NbB sample.

polycrystalline nature [26]. Moreover, the specific surface area (SSA) and pore size distributions of the NbB sample are analyzed by BET test. Fig. 2j shows the type-IV N<sub>2</sub> adsorption–desorption curves with a SSA of 53.9 m<sup>2</sup> g<sup>-1</sup> [27]. The inset curves of pore size distributions exhibit mesoporous characteristics. Large SSA can increase the contact area of electrolyte and electrodes, which provides a favorable way for ion and electron transport. The valence states of elements of NbB sample are characterized through X-ray photoelectron spectroscopy (XPS) analysis. Fig. S1 presents the XPS full spectrum of NbB sample, in which the O element is caused by inevitable oxidation on the surface [28]. In Fig. 2k, the Nb 3d XPS spectrum is deconvoluted into two peaks about Nb 3d<sub>3/2</sub>

and Nb 3d<sub>5/2</sub>. The Nb 3d<sub>5/2</sub> can be divided into oxidation states corresponding to Nb<sup>5+</sup> and Nb<sup>4+</sup> [29]. In Fig. 2l, the B 1s XPS spectrum can deconvolute into three peaks at 190.9, 188.2 eV and 186.1 eV, which are attributed to the B-O, Nb-B and B-B bond, respectively [30].

The CV profiles of NbB electrode are exhibited in Fig. 3a, in which the first cycle profile shows obvious irreversible peaks at 0.73 V during the reduction scan and 1.2 V during the oxidation scan, which may be related to the formation of solid electrolyte interface film (SEI) and the irreversible reaction of the electrode, and lead to low coulombic efficiency. The pair of redox peaks faded in subsequent cycles. The redox peak couple represents the reaction between Li<sup>+</sup> and Nb<sup>4+</sup>/Nb<sup>5+</sup>. The

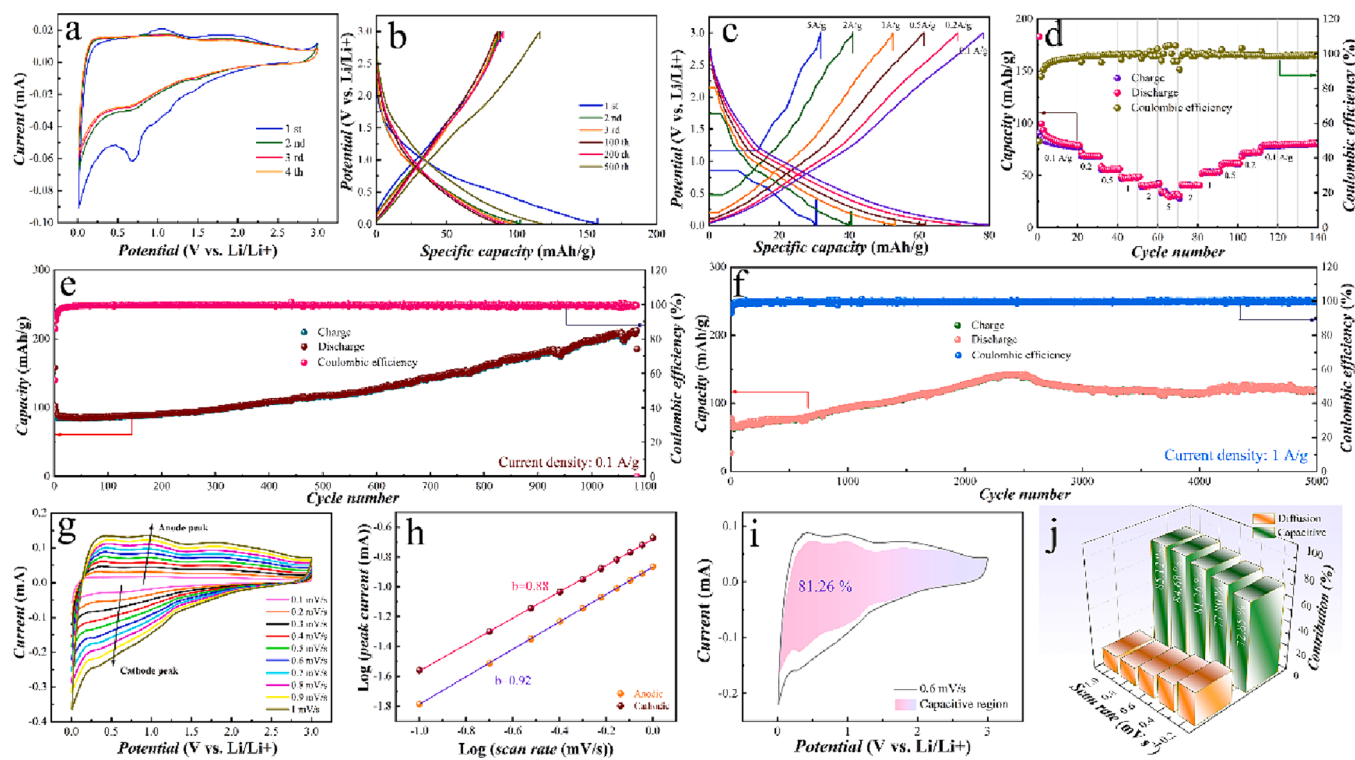


**Fig. 3.** The electrochemical performance of the NbB electrode: (a) CV profiles at  $0.1 \text{ mV s}^{-1}$ , (b) GCD curves at  $0.1 \text{ A g}^{-1}$ , (c-d) GCD curves and rate property, (e-f) cycle durability at  $0.1$  and  $1 \text{ A g}^{-1}$ , respectively, (g) CV profiles, (h)  $\log(i_p)$  vs.  $\log(v)$  plots, (i-j) the diffusion and capacitance contribution at varied scan rate.

GCD plots of NbB electrode are presented in Fig. 3b. The specific capacity of charging and discharging in the first cycle are 88.5 and 157.9  $\text{mAh g}^{-1}$ , respectively, and the coulombic efficiency is 55.89 %. With the increase of the cycle number, specific capacities of electrode decrease first and then increase, indicating the activation process. The GCD profiles in Fig. 3c display the rate property of NbB electrode. The reversible discharge capacity can reach ca. 79.2, 71.7, 61.8, 53.1, 40.6, and 30.6  $\text{mAh g}^{-1}$ , respectively, at  $0.1$  to  $5 \text{ A g}^{-1}$ . As exhibited in Fig. 3d, the discharge specific capacity is restored to 79.5  $\text{mAh/g}$  when the current density is restored to  $0.1 \text{ A g}^{-1}$ . The cycle life of NbB electrode is also tested. The cyclical stability at  $0.1 \text{ A g}^{-1}$  is shown in Fig. 3e. The capacity of the NbB electrode has reduced in the first and then slowly but steadily rose. The decrease in specific capacity may be associated with incomplete electrolyte infiltration, SEI layer formation, and stress change because of lithiation and delithiation [31]. In the following cycles, the  $\text{Li}^+$  diffusion generally due to Li-induced reactivation is enhanced, which leads to an increased capacity. The NbB electrode shows a great capacity of  $197 \text{ mAh g}^{-1}$  for 1000 cycles. In Fig. 3f The cycling life is tested at a high current density of  $1 \text{ A g}^{-1}$ . The specific capacity generally increases over the first 2500 cycles. Analysis shows that the ion diffusion and storage process can be greatly improved by SEI optimization and partial reconstruction of NbB crystal structure. The capacity can reach a stable value of  $118 \text{ mAh g}^{-1}$  for 5000 cycles. The layer crystal structure is satisfactory for effective  $\text{Li}^+$  insertion and extraction, which makes NbB more reversible. The kinetic process of NbB electrode is investigated through Bruce Dunn's method [32]. Fig. 3g presents the CV profiles of NbB anode at various scan rate. The current response can be split into diffusion- and surface capacitive-control reaction processes, which are determined according to Eq. (2) [33]:

$$i_p = av^b \quad (2)$$

When  $b$ -value is verge on 0.5, the current is dominated by diffusion control; when  $b$ -value is verge on 1, it is dominated by surface capacitive control [34]. Fig. 3h reveals the relationship of peak current and scan

rate. The  $b$ -values of NbB are 0.88 and 0.92, which shows that the electrochemical process is controlled by both surface-capacitive and diffusion process [35,36]. The separation of diffusion and capacitance contribution are further studied by Eq. (3) [37]:

$$i(V) = k_1 v + k_2 v^{1/2} \quad (3)$$

where  $k_1$  and  $k_2$  are constant parameters. Fig. 3i-j presents the contribution proportions at various scan rate of NbB electrodes. With the increase of scanning rate, the contribution proportion of surface capacitance also increases. The contribution of surface capacitance is 81.26 % at  $0.6 \text{ mV s}^{-1}$ .

Moreover, the  $\text{Li}^+$  diffusion coefficient ( $D_{\text{Li}}^+$ ) of NbB electrode are further investigated using the electrochemical impedances (EIS) and galvanostatic intermittent titration technique (GITT). Fig. 4a-b display the EIS plots of NbB electrode before cycling and after 100 cycles. The EIS plots show a diagonal line with a long arc, which is related to the Warburg resistance ( $W_o$ ) and charge transfer resistance ( $R_{ct}$ ) [38]. The intercept from the X-axis is the electrolyte resistance ( $R_e$ ). The inset in Fig. 4a shows the equivalent circuit model for the fresh and cycled electrode. The fitting values of  $R_e$  and  $R_{ct}$  before and after electrode cycling are summarized in Table S1. It can be seen that the  $R_e$  value of the electrode increases after cycling, which is related to the SEI layer formed on the surface of the electrode after cycling. The  $R_{ct}$  value decreases significantly, which is associated with the complete infiltration of the electrolyte during cycling, indicating that it has rapid charge transfer. According to the Eqs. (4)–(5) [39]:

$$Z' = R_s + R_{ct} + \sigma \omega^{-1/2} \quad (4)$$

$$D_{\text{Li}^+} = R^2 T^2 / 2A^2 n^4 F^4 C^2 \sigma^2 \quad (5)$$

The  $D_{\text{Li}^+}$  is inversely proportional to the Warburg coefficient ( $\sigma$ ). The parameters are represented gas constant ( $R$ ), absolute temperature ( $T$ ), anode surface area ( $A$ ), transfer electron numbers ( $n$ ), Faraday constant ( $F$ ), and  $\text{Li}^+$  concentration ( $C$ ), respectively. The  $\sigma$  can be obtained by

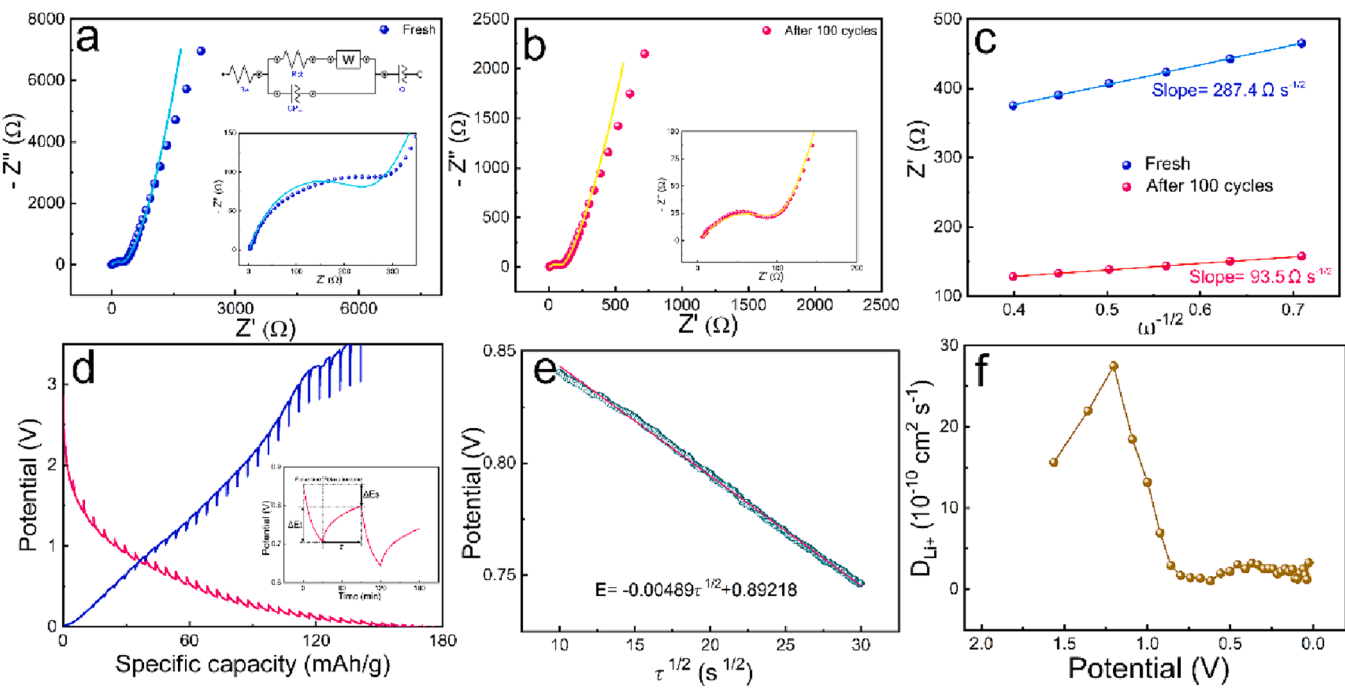


**Fig. 4.** (a-b) EIS curves before and after 100 cycles, (c)  $Z'$  vs.  $\omega^{-1/2}$  curves, (d) GITT curves (inset: a single titration), (e) potential vs.  $\tau^{1/2}$  profiles, (f)  $D_{Li^+}$  of electrode.

fitting the  $\omega^{-1/2}$  vs.  $Z'$  curves [40,41] (Fig. 4c). Before and after cycling, the  $D_{Li^+}$  are calculated to be  $3.7 \times 10^{-12}$  and  $1.1 \times 10^{-11} \text{ cm}^2 \text{s}^{-1}$ , respectively. After cycles, the rate of  $\text{Li}^+$  diffusion is accelerated, leading to a rise in specific capacity. Fig. 4d exhibits the GITT plots of NbB anode, the inset figures show a single titration process. The  $D_{Li^+}$  can be obtained as Eq. (6) [42]:

$$D_{Li^+} = \frac{4}{\pi} \left( \frac{m_B V_M}{M_B S} \right)^2 \left( \frac{\Delta E_s}{\tau (dE_\tau / d\sqrt{\tau})} \right)^2 \left( \tau \ll \frac{L^2}{D_{Li^+}} \right) \quad (6)$$

The parameters are represented the constant current pulse time ( $\tau$ ), the single titration voltage difference ( $\Delta E_s$ ), constant current voltage difference ( $\Delta E_\tau$ ), the mass ( $m_B$ ), molar mass ( $M_B$ ), molar volume ( $V_M$ ), average thickness ( $L$ ) and contact surface area ( $S$ ), respectively. As shown in Fig. 4e, the relationship of  $V$  and  $\tau^{1/2}$  is linear, so the simplified Eq. (5) is Eq. (7) [43,44]:

$$D_{Li^+} = \frac{4}{\pi} \left( \frac{m_B V_M}{M_B S} \right)^2 \left( \frac{\Delta E_s}{\Delta E_\tau} \right)^2 \quad (7)$$

The results in Fig. 4f show that the  $D_{Li^+}$  is changed with the potential during discharging process, and the maximum value of  $D_{Li^+}$  is about  $2.7 \times 10^{-9} \text{ cm}^2 \text{s}^{-1}$ .

The ex-situ XRD and XPS analyses are performed to study the lithium-ion storage mechanism of NbB anode. Fig. 5a presents the ex-situ XRD pattern of NbB anode with different charge and discharge potential at  $0.1 \text{ A g}^{-1}$  during the 2nd discharging-charging process. All of the XRD patterns are consistent with the card of NbB and no other diffraction peaks appear, which demonstrates that the charge storage stems from intercalation reaction [45]. Besides, the diffraction peak angle attributed to the (021) crystal plane decreases during the discharge, which means that  $\text{Li}^+$  is embedded in the layer of the NbB crystal structure. The angle of the diffraction peak increases during the charge, which is related to the extraction of  $\text{Li}^+$  [46]. Fig. 5b is the schematic diagram of the intercalation-type NbB electrode during charge and discharge. The ex-situ XPS is used to study the surface elemental valence state of the electrode at the voltage of 0.01 V (fully discharged) and 3.0 V (fully charged). The Nb 3d spectra (Fig. 5c) show three peaks at 204.3, 206.5 and 208.9 eV at the voltage of 0.01 V.

Compared to fresh NbB sample, the decrease in binding energy is due to the reduction of the  $\text{Nb}^{+5}$  or  $\text{Nb}^{+4}$  to the  $\text{Nb}^{+4}$  or  $\text{Nb}^{+2}$  with the insertion of  $\text{Li}^+$ . Under the voltage of 3.0 V, the binding energy of the Nb 3d spectrum increased, corresponding to the extraction of  $\text{Li}^+$ . In Fig. 5d, the B 1s spectra at both 0.01 V and 3.0 V show two peaks corresponding to the B-O and Nb-B bond without obvious shift, which suggests that the B species are inert during the redox process [47]. Compared to the initial B 1s spectrum, the B-B bond disappears, which is related to the formation of the SEI film. In Fig. 5e, the appearance of the Li 1s peak also proves that the SEI layer is formed on the surface of the NbB electrode. Compared with the Li signal at 0.01 V, the intensity of the Li signal at 3.0 V is obviously weakened, which indicates that part of  $\text{Li}^+$  is removed from the NbB electrode.

Figs. S2-S3 show the XRD pattern and  $N_2$  adsorption-desorption isotherms of AC material. The AC shows a large specific surface area of  $2368.7 \text{ m}^2 \text{ g}^{-1}$ . The electrochemical properties of the AC electrode are exhibited in Figs. S4-S7. The NbB//AC LICs are constructed with NbB as anode and AC as cathode, and the illustration is shown in Fig. 6a. To investigate the effect of the testing voltage window on the electrochemical performance of the device, tests are conducted under voltage windows of 2.2–3.8 V, 1.5–4.0 V, 0.5–4.0 V, and 0.1–4.0 V, with the corresponding devices designated as NbB//AC LIC-1, NbB//AC LIC-2, NbB//AC LIC-3, and NbB//AC LIC-4, respectively. Fig. 6b-c, Fig. S8, Fig. S10, and Fig. S12 show the CV curves of the devices under different voltage windows. It can be observed that the best match between the battery-type anode and the capacitive cathode occurs within the potential window of 2.2–3.8 V, exhibiting a rectangular shape without polarization at high potentials. Fig. 6d, Fig. S9, Fig. S11, and Fig. S13 present the GCD curves of the devices under different voltage windows. There are significant IR-drop during testing, during the test, which caused the GCD curve to exhibit asymmetric behavior, resulting in reduced energy efficiency (Table S2). Based on the GCD curves, the specific capacitances of the devices are calculated and the results are presented in Fig. 6e. At  $0.05 \text{ A g}^{-1}$ , the specific capacitances of NbB//AC LIC-1, NbB//AC LIC-2, NbB//AC LIC-3, and NbB//AC LIC-4 are 28.1, 26.0, 21.8, and  $34.7 \text{ F g}^{-1}$ , respectively. However, when tested at higher current densities, significant capacitance losses occur due to the imbalance in power capabilities between the anode and cathode

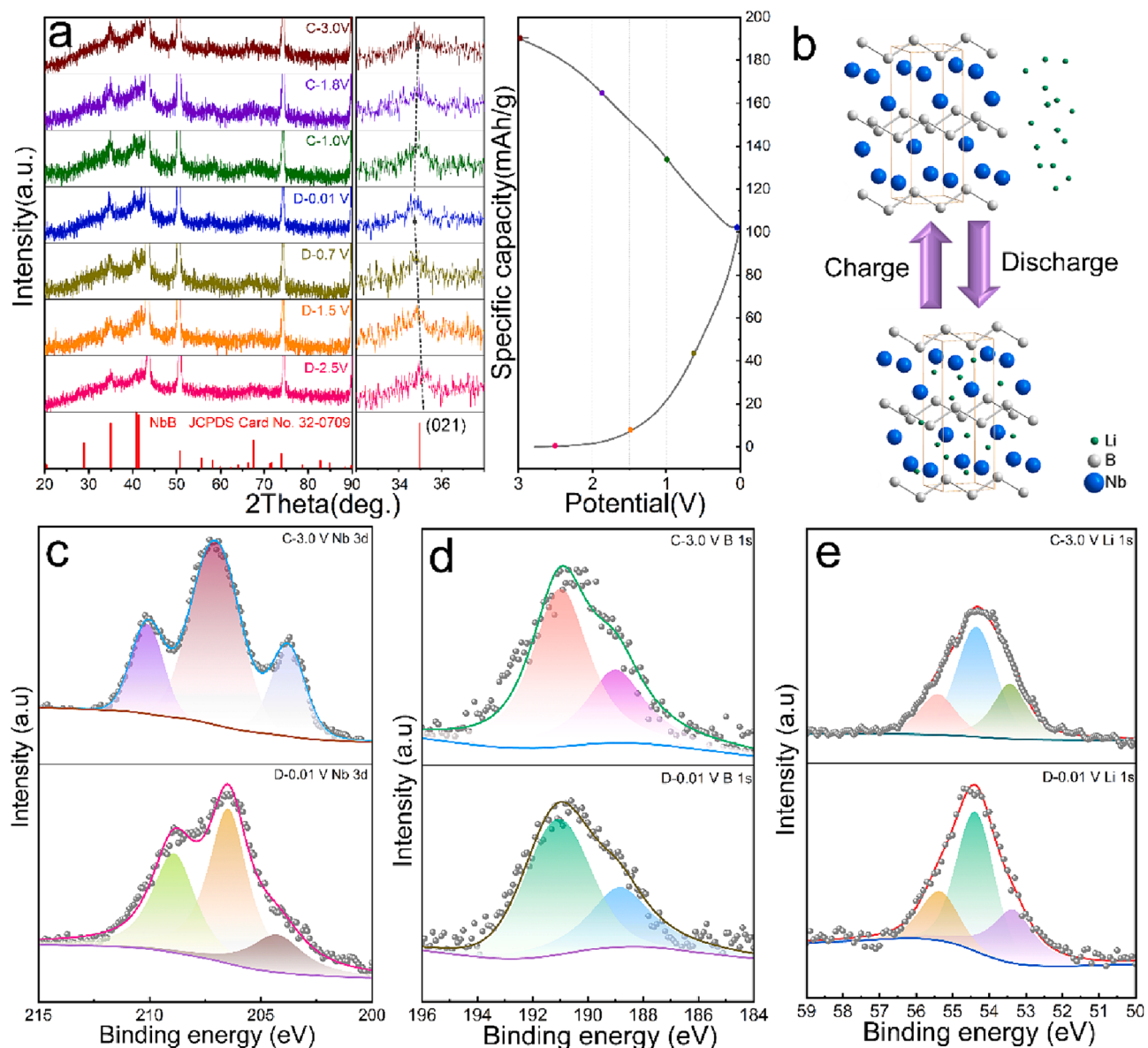


**Fig. 5.** (a) Ex-situ XRD pattern at different potential, (b) illustration of Li<sup>+</sup> insertion and extraction, (c-e) ex-situ XPS spectra at 0.01 V and 3.0 V.

electrodes. Generally, the wide potential range can increase the energy density, but it will reduce the cycle stability [48]. Fig. 6f illustrates the power density and energy density of the NbB//AC LICs. It can be seen that NbB//AC LIC-4 exhibits high energy and power, with an energy density of 73.4 Wh kg<sup>-1</sup> at 97.5 W kg<sup>-1</sup> and a power density of 4.68 kW kg<sup>-1</sup> at 24.2 Wh kg<sup>-1</sup>, surpassing some reported LIC devices[49–52]. Nevertheless, in Fig. 6f and Fig. S14, NbB//AC LIC-1 demonstrates superior cycling stability, with a capacitance retention rate of 70 % after 13,000 cycles, higher than the 60 % retention rate of the NbB//AC LIC-4 device.

### 3. Conclusion

In a word, a novel electrode material for lithium-ion capacitor anode is reported. The pure-phase NbB nanoparticles are successfully synthesized in NaCl-KCl molten salts with Nb<sub>2</sub>O<sub>5</sub> and B powders as ingredients. The crystallinity, elemental composition, valence, morphology and SSA of the NbB sample are explored through various advanced characterization techniques. The high SSA of NbB increases the contact area of the electrolyte and electrode. More importantly, its layer crystal structure

provides a favorable way for lithiation and delithiation, resulting in a fast and efficient kinetic process. It can maintain a specific capacity of 197 mAh g<sup>-1</sup> at 0.1 A g<sup>-1</sup> after 1000 cycles. Upon increasing the rate to 1 A g<sup>-1</sup>, the high capacity of 118 mAh/g can be maintained for 5000 cycles. Further ex-situ XRD and XPS tests show that NbB electrode has the intercalation-type Li<sup>+</sup> storage mechanism. In addition, the assembled NbB// AC LIC-1 has great specific capacitance, and 70 % capacitance retention for 12,000 cycles. The results of these studies prove that the prospects for developing high-performance and practically viable LICs with TMBs anode are promising.

### CRediT authorship contribution statement

**Jing-Feng Hou:** Writing – review & editing, Writing – original draft, Investigation, Data curation. **Jian-Fei Gao:** Validation, Methodology, Conceptualization. **Ling-Bin Kong:** Supervision, Resources, Project administration, Funding acquisition.

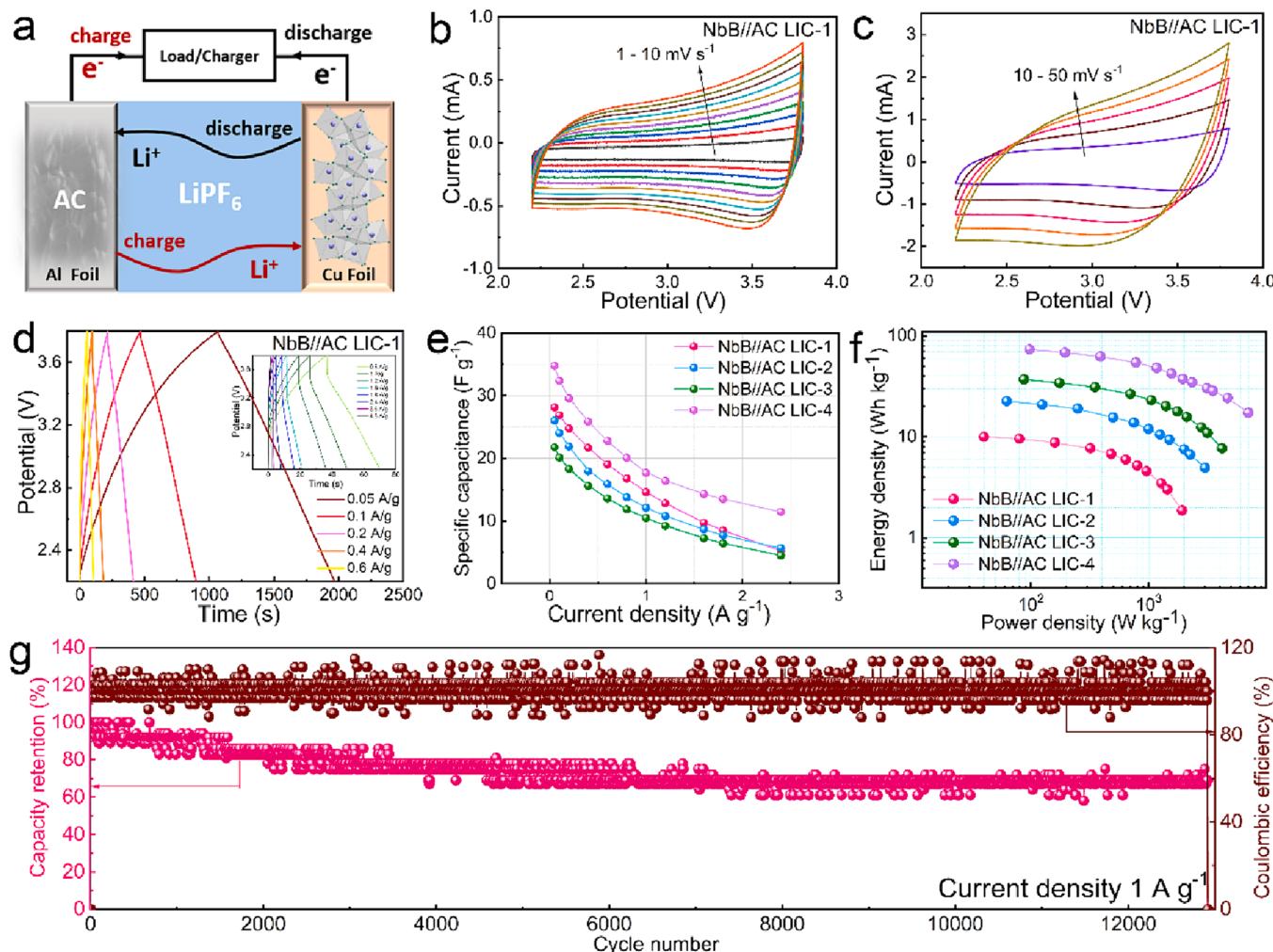


**Fig. 6.** The electrochemical characterizations of NbB//AC LIC: (a) illustration of the LICs, (b-c) CV curves of NbB//AC LIC-1, (d) GCD curves of NbB//AC LIC-1, (e) rate property, (f) Ragone plots, (g) cycling stability at 1 A g<sup>-1</sup> of NbB//AC LIC-1.

#### Declaration of competing interest

The authors declare that they have no known competing financial interests or personal relationships that could have appeared to influence the work reported in this paper.

#### Acknowledgments

This work was supported by the National Natural Science Foundation of China (No. 52261040, 51971104) and the Major Science and Technology Project of Gansu Province (22ZD6GA008).

#### Appendix A. Supplementary data

Supplementary data to this article can be found online at <https://doi.org/10.1016/j.jelechem.2024.118274>.

#### References

- [1] D.P. Ojha, H.P. Karki, J.H. Song, H.J. Kim, Decoration of g-C<sub>3</sub>N<sub>4</sub> with hydrothermally synthesized FeWO<sub>4</sub> nanorods as the high-performance supercapacitors, *Chem. Phys. Lett.* 712 (2018) 83–88.
- [2] L. Zhang, X. Qin, S. Zhao, A. Wang, J. Luo, Z.L. Wang, F. Kang, Z. Lin, B. Li, Advanced matrices for binder-free nanostructured electrodes in lithium-ion batteries, *Adv. Mater.* 32 (24) (2020) 1908445.
- [3] J. Wang, Z. Yan, G. Yan, H. Guo, X. Li, Z. Wang, X. Wang, Z. Yang, Spiral graphene coupling hierarchically porous carbon advances dual-carbon lithium ion capacitor, *Energy Storage Mater.* 38 (2021) 528–534.
- [4] X. Ding, H. Huang, Q. Huang, B. Hu, X. Li, X. Ma, X. Xiong, Doping sites modulation of T-Nb<sub>2</sub>O<sub>5</sub> to achieve ultrafast lithium storage, *J. Energy Chem.* 77 (2023) 280–289.
- [5] M.-S. Park, Y.-G. Lim, J.-H. Kim, Y.-J. Kim, J. Cho, J.-S. Kim, A Novel lithium-doping approach for an advanced lithium ion capacitor, *Adv. Energy Mater.* 1 (6) (2011) 1002–1006.
- [6] F.-F. Li, J.-F. Gao, Z.-H. He, L.-B. Kong, Crystal phase-controlled synthesis of the CoP@Co<sub>2</sub>P heterostructure with 3D nanowire networks for high-performance Li-ion capacitor applications, *ACS Appl. Mater. Interfaces* 13 (8) (2021) 10071–10088.
- [7] M.V. Reddy, G.V. Subba Rao, B.V.R. Chowdari, Metal oxides and oxysalts as anode materials for Li ion batteries, *Chem. Rev.* 113 (7) (2013) 5364–5457.
- [8] Y. Hao, S. Wang, Y. Shao, Y. Wu, S. Miao, High-energy density Li-ion capacitor with layered sns<sub>2</sub>/reduced graphene oxide anode and BCN nanosheet cathode, *Adv. Energy Mater.* 10 (6) (2020) 1902836.
- [9] L. Shen, H. Lv, S. Chen, P. Kopold, P.A. van Aken, X. Wu, J. Maier, Y. Yu, Peapod-like Li<sub>3</sub>VO<sub>4</sub>/N-Doped carbon nanowires with pseudocapacitive properties as advanced materials for high-energy lithium-ion capacitors, *Adv. Mater.* 29 (27) (2017) 1700142.
- [10] X. Wang, L. Liu, Z. Niu, Carbon-based materials for lithium-ion capacitors, *Mater. Chem. Front.* 3 (7) (2019) 1265–1279.
- [11] S.S. Zhang, Dual-Carbon Lithium-Ion Capacitors: Principle, Materials, and Technologies, *Batteries & Supercaps* 3(11) (2020) 1137–1146.
- [12] Y. Xiang, P. Zhao, Z. Jin, B. Chen, H. Ming, H. Zhang, W. Zhang, G. Cao, X. Zhu, Three-dimensional and mesopore-oriented graphene conductive framework anchored with nano-Li<sub>4</sub>Ti<sub>5</sub>O<sub>12</sub> Particles as an ultrahigh rate anode for lithium-ion batteries, *ACS Appl. Mater. Interfaces* 10 (49) (2018) 42258–42267.
- [13] H. Yan, D. Zhang, X. Qilu, X.S. Duo, A review of spinel lithium titanate (Li<sub>4</sub>Ti<sub>5</sub>O<sub>12</sub>) as electrode material for advanced energy storage devices, *Ceram. Int.* 47 (5) (2021) 5870–5895.
- [14] G. Wang, J. Zhang, S. Yang, F. Wang, X. Zhuang, K. Müllen, X. Feng, Vertically aligned MoS<sub>2</sub> nanosheets patterned on electrochemically exfoliated graphene for

- high-performance lithium and sodium storage, *Adv. Energy Mater.* 8 (8) (2018) 1702254.
- [15] G. Zhu, L. Ma, H. Lin, P. Zhao, L. Wang, Y. Hu, R. Chen, T. Chen, Y. Wang, Z. Tie, Z. Jin, High-performance Li-ion capacitor based on black-TiO<sub>2-x</sub>/graphene aerogel anode and biomass-derived microporous carbon cathode, *Nano Res.* 12 (7) (2019) 1713–1719.
- [16] R. Wang, S. Wang, D. Jin, Y. Zhang, Y. Cai, J. Ma, L. Zhang, Engineering layer structure of MoS<sub>2</sub>-graphene composites with robust and fast lithium storage for high-performance Li-ion capacitors, *Energy Storage Mater* 9 (2017) 195–205.
- [17] L. Jing, G. Lian, F. Niu, J. Yang, Q. Wang, D. Cui, C.-P. Wong, X. Liu, Few-atomic-layered hollow nanospheres constructed from alternate intercalation of carbon and MoS<sub>2</sub> monolayers for sodium and lithium storage, *Nano Energy* 51 (2018) 546–555.
- [18] W. Li, X. Sun, Y. Yu, Si-, Ge-, Sn-based anode materials for lithium-ion batteries: from structure design to electrochemical performance, *Small Methods* 1 (3) (2017) 1600037.
- [19] H. Wu, Y. Cui, Designing nanostructured Si anodes for high energy lithium ion batteries, *Nano Today* 7 (5) (2012) 414–429.
- [20] H. Chen, X. Zou, Intermetallic borides: structures, synthesis and applications in electrocatalysis, *Inorg. Chem. Front.* 7 (11) (2020) 2248–2264.
- [21] A. Thakur, A. Rasyotra, K. Jasuja, Review and perspectives of electrochemical energy conversion and storage in metal diborides and XBenes, *Energy Fuel* 37 (23) (2023) 18310–18329.
- [22] H. Aydin, Ü. Kurtan, B. Üstün, S.N. Koç, E. Akgül, M. Demir, A review on the recent advancement of metal-boride derived nanostructures for supercapacitors, *J. Storage Mater.* 72 (2023) 108306.
- [23] R.K. Tripathy, A.K. Samantara, J.N. Behera, Metal-organic framework (MOF)-derived amorphous nickel boride: an electroactive material for electrochemical energy conversion and storage application, *Sustainable Energy Fuels* 5 (4) (2021) 1184–1193.
- [24] S. Suriyakumar, A. Varma, V. Surendran, K. Jasuja, M.M. Shajumon, Nanosheets derived through dissolution-recrystallization of TiB<sub>2</sub> as efficient anode for sodium-ion batteries, *Batteries & Supercaps* 5 (2) (2022) e202100243.
- [25] S. Ran, H. Sun, Y.N. Wei, D. Wang, N. Zhou, Q. Huang, Low-Temperature Synthesis of Nanocrystalline NbB<sub>2</sub> Powders by Borothermal Reduction in Molten Salt, *J. Am. Ceram. Soc.* 97 (11) (2014) 3384–3387.
- [26] B. Wang, L. Wang, B. Zhang, S. Zeng, F. Tian, J. Dou, Y. Qian, L. Xu, Niobium diboride nanoparticles accelerating polysulfide conversion and directing Li<sub>2</sub>S nucleation enabled high areal capacity lithium-sulfur batteries, *ACS Nano* 16 (3) (2022) 4947–4960.
- [27] X. Liu, Y. Gong,  $\alpha$ -MoB<sub>2</sub> nanosheets for hydrogen evolution in alkaline and acidic media, *ACS Appl. Nano Mater.* 5 (8) (2022) 10183–10191.
- [28] G. Gouget, D.P. Debecker, A. Kim, G. Olivieri, J.-J. Gallet, F. Bourrel, C. Thomas, O. Ersen, S. Moldovan, C. Sanchez, S. Carencio, D. Portehault, In Situ solid-gas reactivity of nanoscaled metal borides from molten salt synthesis, *Inorg. Chem.* 56 (15) (2017) 9225–9234.
- [29] K. Kim, M.-S. Kim, P.-R. Cha, S.H. Kang, J.-H. Kim, Structural modification of self-organized nanoporous niobium oxide via hydrogen treatment, *Chem. Mater.* 28 (5) (2016) 1453–1461.
- [30] X. Liu, Y. Gong, A simple molten salt route to crystalline  $\beta$ -MoB<sub>2</sub> nanosheets with high activity for the hydrogen evolution reaction, *Inorg. Chem.* 60 (23) (2021) 18075–18081.
- [31] W. Zhu, S.A. El-Khodary, S. Li, B. Zou, R. Kang, G. Li, D.H.L. Ng, X. Liu, J. Qiu, Y. Zhao, Y. Huang, J. Lian, H. Li, Roselle-like Zn<sub>2</sub>Ti<sub>3</sub>O<sub>8</sub>/rGO nanocomposite as anode for lithium ion capacitor, *Chem. Eng. J.* 385 (2020) 123881.
- [32] C. Choi, D.S. Ashby, D.M. Butts, R.H. DeBlock, Q. Wei, J. Lau, B. Dunn, Achieving high energy density and high power density with pseudocapacitive materials, *Nat. Rev. Mater.* 5 (1) (2020) 5–19.
- [33] Z. Zheng, H.-H. Wu, H. Liu, Q. Zhang, X. He, S. Yu, V. Petrova, J. Feng, R. Kostecki, P. Liu, D.-L. Peng, M. Liu, M.-S. Wang, Achieving fast and durable lithium storage through amorphous FeP nanoparticles encapsulated in ultrathin 3D P-doped porous carbon nanosheets, *ACS Nano* 14 (8) (2020) 9545–9561.
- [34] H. Lindström, S. Södergren, A. Solbrand, H. Rensmo, J. Hjelm, A. Hagfeldt, S.-E. Lindquist, Li<sup>+</sup> ion insertion in TiO<sub>2</sub> (Anatase). 2. Voltammetry on nanoporous films, *J. Phys. Chem. B* 101 (39) (1997) 7717–7722.
- [35] S. Li, Y. Cui, R. Kang, B. Zou, D.H.L. Ng, S.A. El-Khodary, X. Liu, J. Qiu, J. Lian, H. Li, Oxygen vacancies boosted the electrochemical kinetics of Nb<sub>2</sub>O<sub>5-x</sub> for superior lithium storage, *Chem. Commun.* 57 (66) (2021) 8182–8185.
- [36] W. Zhu, B. Zou, C. Zhang, D.H.L. Ng, S.A. El-Khodary, X. Liu, G. Li, J. Qiu, Y. Zhao, S. Yang, J. Lian, H. Li, Oxygen-defective TiNb<sub>2</sub>O<sub>7-x</sub> nanochains with enlarged lattice spacing for high-rate lithium ion capacitor, *Adv. Mater. Interfaces* 7 (16) (2020) 2000705.
- [37] B.-M. Zhang, C.-B. Zhang, H. Zhang, Y.-X. Hu, Y.-S. Zhang, C. Lu, J. Li, L.-B. Kong, M.-C. Liu, Three-dimensional honeycomb-like MoSe<sub>2</sub>/rGO as high performance sodium ions storage materials with long cycle stability and high rate capability, *Appl. Surf. Sci.* 513 (2020) 14582.
- [38] S. Wang, L. Li, Y. Shao, L. Zhang, Y. Li, Y. Wu, X. Hao, Transition-Metal oxynitride: A facile strategy for improving electrochemical capacitor storage, *Adv. Mater.* 31 (10) (2019) 1806088.
- [39] X. Yang, Q. Li, H. Wang, J. Feng, M. Zhang, R. Yuan, Y. Chai, In-situ carbonization for template-free synthesis of MoO<sub>2</sub>-Mo<sub>2</sub>C microspheres as high-performance lithium battery anode, *Chem. Eng. J.* 337 (2018) 74–81.
- [40] S.A. El-Khodary, G. Subburam, B.-B. Zou, J. Wang, J.-X. Qiu, X.-H. Liu, D.H.L. Ng, S. Wang, J.-B. Lian, Mesoporous silica anchored on reduced graphene oxide nanocomposite as anode for superior lithium-ion capacitor, *Rare Met.* 41 (2) (2022) 368–377.
- [41] Z. Zhou, M. Han, Y. Sun, Y. Cui, S.A. El-khodary, D.H.L. Ng, J. Lian, J. Ma, Zinc-ion and proton as joint charge carriers of S-MoO<sub>2</sub> for high-capacity aqueous zinc-ion batteries, *Adv. Funct. Mater.* 34 (7) (2024) 2308834.
- [42] F.-F. Li, J.-F. Gao, Z.-H. He, N. Brandon, X. Li, L.-B. Kong, Engineering novel Ni<sub>2</sub>-XCo<sub>x</sub>P structures for high performance lithium-ion storage, *Energy Storage Mater* 48 (2022) 20–34.
- [43] X. Li, X. Wang, W. Yang, Z. Zhu, R. Zhao, Q. Li, H. Li, J. Xu, G. Zhao, H. Li, S. Li, Three-dimensional hierarchical flowerlike FeP wrapped with N-doped carbon possessing improved Li<sup>+</sup> diffusion kinetics and cyclability for lithium-ion batteries, *ACS Appl. Mater. Interfaces* 11 (43) (2019) 39961–39969.
- [44] Y. Xu, X. Li, J. Wang, Q. Yu, X. Qian, L. Chen, Y. Dan, Fe-doped CoP flower-like microstructure on carbon membrane as integrated electrode with enhanced sodium ion storage, *Chemistry – A European Journal* 26 (6) (2020) 1298–1305.
- [45] B. Zou, T. Wang, S. Li, R. Kang, G. Li, S.A. El-Khodary, D.H.L. Ng, X. Liu, J. Qiu, Y. Zhao, J. Lian, H. Li, In situ XRD and electrochemical investigation on a new intercalation-type anode for high-rate lithium ion capacitor, *Journal of Energy, Chemistry* 57 (2021) 109–117.
- [46] Z. Song, H. Li, W. Liu, H. Zhang, J. Yan, Y. Tang, J. Huang, H. Zhang, X. Li, Ultrafast and stable Li-(De)intercalation in a large single crystal H-Nb<sub>2</sub>O<sub>5</sub> anode via optimizing the homogeneity of electron and ion transport, *Adv. Mater.* 32 (22) (2020) 2001001.
- [47] A.A. Rezaie, Z. Yan, J.P. Scheifers, J. Zhang, J. Guo, B.P.T. Fokwa, Synthesis and Li-ion electrode properties of layered MAB phases  $\text{Nin+1ZnBn}$  ( $n = 1, 2$ ), *J. Mater. Chem. A* 8 (4) (2020) 1646–1651.
- [48] A. Lu, X. Zhang, Y. Chen, Q. Xie, Q. Qi, Y. Ma, D.-L. Peng, Synthesis of Co<sub>2</sub>P/graphene nanocomposites and their enhanced properties as anode materials for lithium ion batteries, *J. Power Sources* 295 (2015) 329–335.
- [49] C. Lu, X. Wang, X. Zhang, H. Peng, Y. Zhang, G. Wang, Z. Wang, G. Cao, N. Umirov, Z. Bakarov, Effect of graphene nanosheets on electrochemical performance of Li<sub>4</sub>Ti<sub>5</sub>O<sub>12</sub> in lithium-ion capacitors, *Ceram. Int.* 43 (8) (2017) 6554–6562.
- [50] S. Fleischmann, M. Zeiger, A. Quade, A. Kruth, V. Presser, Atomic layer-deposited molybdenum oxide/carbon nanotube hybrid electrodes: the influence of crystal structure on lithium-ion capacitor performance, *ACS Appl. Mater. Interfaces* 10 (22) (2018) 18675–18684.
- [51] P. Yu, G. Cao, S. Yi, X. Zhang, C. Li, X. Sun, K. Wang, Y. Ma, Binder-free 2D titanium carbide (MXene)/carbon nanotube composites for high-performance lithium-ion capacitors, *Nanoscale* 10 (13) (2018) 5906–5913.
- [52] X. Jiao, Q. Hao, X. Xia, Z. Wu, W. Lei, Metal organic framework derived Nb<sub>2</sub>O<sub>5</sub>@C nanoparticles grown on reduced graphene oxide for high-energy lithium ion capacitors, *Chem. Commun.* 55 (18) (2019) 2692–2695.